Fabrication of ZnCoS nanomaterial for high energy flexible asymmetric supercapacitors

Yuan Zhang, Ning Cao, Sabine Szunerits, Ahmed Addad, Pascal Roussel, Rabah Boukherroub

To cite this version:

Yuan Zhang, Ning Cao, Sabine Szunerits, Ahmed Addad, Pascal Roussel, et al.. Fabrication of ZnCoS nanomaterial for high energy flexible asymmetric supercapacitors. Chemical Engineering Journal, 2019, 374, pp.347-358. 10.1016/j.cej.2019.05.181 . hal-02263480

HAL Id: hal-02263480

https://hal.science/hal-02263480

Submitted on 23 Aug 2021

Facile fabrication of ZnCoS nanomaterial for high energy flexible asymmetric supercapacitor devices

Yuan Zhang[1,#], Ning Cao[2,3,#] , Sabine Szunerits[1], Ahmed Addad,[4] Pascal Roussel[5] and Rabah Boukherroub[1*]

[1]Univ. Lille, CNRS, Centrale Lille, ISEN, Univ. Valenciennes, UMR 8520 - IEMN, F-59000 Lille, France
[2]Key Laboratory of Unconventional oil & Gas Development, China University of Petroleum (East China), Qingdao 266580, P.R. China
[3]School of Materials Science and Engineering, China University of Petroleum (East China), Qingdao, Shandong Province, 266580, P. R. China
[4]Univ. Lille, CNRS, UMR 8207 – UMET, F-59000 Lille, France
[5]Univ. Lille, CNRS, ENSCL, Centrale Lille, Univ. Artois, UMR8181, UCCS-Unité de Catalyse et Chimie du Solide, Lille, F-59000, France

---

[#] Both authors have equally contributed.

[*]To whom correspondence should be send to : rabah.boukherroub@univ-lille.fr; Tel:+33 (0)362531724; Fax: Tel:+33 (0)362531701

Abstract

Bimetal sulfides as anode electrode materials have attracted extensive attention owing to their superior electrochemical activity compared to their mono-metal sulfide counterparts. Herein, ZnCoS nanomaterial was synthesized by chemical precipitation and ion-exchange process. The obtained ZnCoS can be considered as the product of partial substitution of Zn^{2+} by Co^{2+} and/or Co^{3+} ions in the ZnS lattice. Benefiting from the synergistic effects, the ZnCoS was evaluated as electrode material for supercapacitors. By varying the preparation conditions, we found that the ZnCoS material synthesized using an initial mole ratio of Co/Zn = 2 at 50 °C gave the best performance with a maximum specific capacitance of 1134.7 F g^{-1} at 1 A g^{-1}, which is about 7.7 times that of bare ZnS electrode material. Furthermore, this electrode material exhibits good rate capability (81% retention from 1 to 20 A g^{-1}) and excellent cycling stability with no obvious specific capacitance decrease at 20 A g^{-1} after 6000 charging-discharging cycles. A fabricated flexible asymmetric supercapacitor, consisting of ZnCoS and porous reduced graphene oxide, displays a maximum specific capacitance of about 90 F g^{-1} at 10 mV s^{-1} with an energy density of 17.7 W h kg^{-1} at a power density of 435 W kg^{-1}.

Keywords: *ZnCoS, Chemical precipitation; Ion exchange; Anode; Supercapacitors; Flexible ASC device.*

1. Introduction

With the ever-growing demand for global energy caused by the consumption of fossil fuels[1-3], it becomes urgent and mandatory for searching alternative renewable energy resources, and energy conversion and storage devices [4]. In the field of energy storage, supercapacitors (SCs) have generated substantial attention owing to their larger specific capacity compared to traditional capacitors, high power storage capability, and much higher charging and discharging rate capability efficiency than primary/secondary batteries [4-7]. These advantages propel SCs devices at the forefront of growth in mobile electronic devices, smart grids, and so on. Thus, the last decades have witnessed significant developments on improving the specific capacitance of supercapacitors. According to previous literature reports [5, 8-11], the nature and composition of electrode materials used in SCs devices play a dominant role in the capacitance and charge storage ability. Up to date, a huge attention has been paid on the design and synthesis of pseudocapacitive electrode materials due to their promising electrochemical performance such as multiple oxidation states and high electrochemical activity [12-17].

Owing to their reversible faradic redox reactions, metal sulfides such as NiS [18-19], CoS [20-21] and ZnS [22-24] electrodes are expected to provide a much higher specific capacitance than traditional carbon materials. Therefore, they have been considered as promising anode materials for the next-generation supercapacitors. Among them, ZnS, a wide band gap material (3.5-3.8 eV), has attracted a huge attention in the field of energy storage [23-24]. However, ZnS-based materials face some limitations, such as low specific capacitance and poor conductivity for practical commercial usage [25]. According to previous studies, the combination of various sulfides, such as NiCoS [26-28], $CuCo_2S_4$ [29] and MnCoS [30] has been regarded as one of the most feasible ways to obtain an enhancement of the electrochemical performance because of richer redox reactions occurring during the charging and discharging processes. Based on recent reports, Co-based sulfides demonstrate a high theoretical specific capacitance [31-32]. Therefore, in this study, we investigate the electrochemical properties of ZnCoS, prepared by an easy method, as an anode in supercapacitors. By introducing of cobalt into Zn-based sulfides, it is expected to achieve an improved electrochemical performance.

In this work, ZnCoS materials were successfully obtained *via* the combination of chemical precipitation and ion-exchange processes. First, a bimetallic Zn-Co based precursor was prepared in an aqueous solution at different temperatures, followed by an oil bath ion-exchange sulfurization route to transform Zn-Co precursor into ZnCoS. The synthesized material using a molar ratio Zn: Co (1:2) synthesized at 50 °C delivered a high specific capacitance of 1134.7 F g^{-1} at 1 A g^{-1} together with a good rate capability (81% retention from 1 to 20 A g^{-1}), and a good rate capability with no obvious decrease of the capacity at a current density of 20 A g^{-1} after 6000 charging-discharging cycles, making this novel electrode material ideal anode for supercapacitors.

2. Experimental section

2.1. Materials

Ammonia solution (NH_3•H_2O), potassium hydroxide (KOH), poly(*N*-vinylpyrrolidone) (PVP), *N*-methyl-2-pyrrolidone (NMP), zinc acetate dihydrate ($Zn(CH_3COO)_2$•$2H_2O$), cobalt dichloride hexahydrate ($CoCl_2$•$6H_2O$), thioacetamide (TAA), potassium permanganate ($KMnO_4$), hydrazine monohydrate ($NH_2NH_2 \times H_2O$), hydrochloric acid (HCl), hydrogen peroxide (H_2O_2, 30%), graphite powder (<20 micrometers), sulfuric acid (H_2SO_4), sodium nitrate ($NaNO_3$), ethanol (CH_3CH_2OH), and polyvinylidene fluoride (PVDF) were obtained from Sigma–Aldrich. All materials are used without any further purification.

Nickel foam (NF), obtained from Jiayisheng Company (China), was used as a current collector.

2.2. Synthesis of ZnS and ZnCoS nanoparticles

2.2.1. Synthesis of ZnS

ZnS synthesis was achieved using the following procedure. Two different solutions were prepared separately: a solution A by dissolving at room temperature 1g of PVP in 15 mL Milli-Q water, and a solution B by dissolving 660 mg of $Zn(CH_3COO)_2$•$2H_2O$ in 15 mL Milli-Q water. After mixing the solutions A and B, 286.5 μL ammonia (35%) were dropped into the solution under strong magnetic stirring and kept overnight to yield a precipitate. The precipitate was rinsed sequentially with ethanol and Milli-Q water until the pH was ~7. The resulting product was re-dispersed in Milli-Q water (30 mL) for further use.

A homogeneous solution of thioacetamide (TAA, 100 mg) in 10 mL Milli-Q water was mixed with 10 mL of the above solution under vigorous magnetic stirring. The resulting mixture was heated at 130 °C for 5 h, after which a black solid is formed. The resulting black precipitate was separated through centrifugation, rinsed with ethanol and Milli-Q water, and dried in an oven at 60 °C overnight. The sample was referred to as Zn: Co (1:0) RT. RT stands for room temperature at which the precipitation process was performed.

2.2.2. Synthesis of ZnCoS nanoparticles

ZnCoS nanoparticles were synthesized using a similar procedure (Fig. 1). A solution A consisting of 1 g PVP and 15 mL Milli-Q water, and a solution B made up of different mole ratios of $Zn(CH_3COO)_2 \cdot 2H_2O$ and $CoCl_2 \cdot 6H_2O$ (the total amount of both precursors is fixed at 3 mmol) were prepared. After mixing solutions A and B, 286.5 μL ammonia (35%) were dropped into the mixture and maintained overnight at a certain temperature. A precipitate was formed and rinsed copiously with ethanol and Milli-Q water until the pH ~7. The resulting product was re-dispersed in Milli-Q water (30 mL) for further use.

After a similar ion-exchange process, samples were obtained and labeled based on the initial mole ratio of the Zn and Co precursors and the temperature during the chemical precipitation process. For example, the sample Zn: Co (1:2) 50 means that the initial mole ratio of the precursor of Zn and Co was 1:2, and the chemical precipitation temperature is 50 °C. The preparation conditions of ZnCoS electrode materials are depicted in Table 1.

Table 1. Preparation conditions of ZnCoS samples.

Sample	Initial mole ratio of Zn/Co	Temperature during chemical precipitation process (°C)
Zn:Co (1:0) RT	1:0	RT
Zn:Co (1:1) RT	1:1	RT
Zn:Co (1:2) RT	1:2	RT
Zn:Co (1:3) RT	1:3	RT
Zn:Co (0:1) RT	0:1	RT
Zn:Co (1:2) 50	1:2	50
Zn:Co (1:2) 80	1:2	80

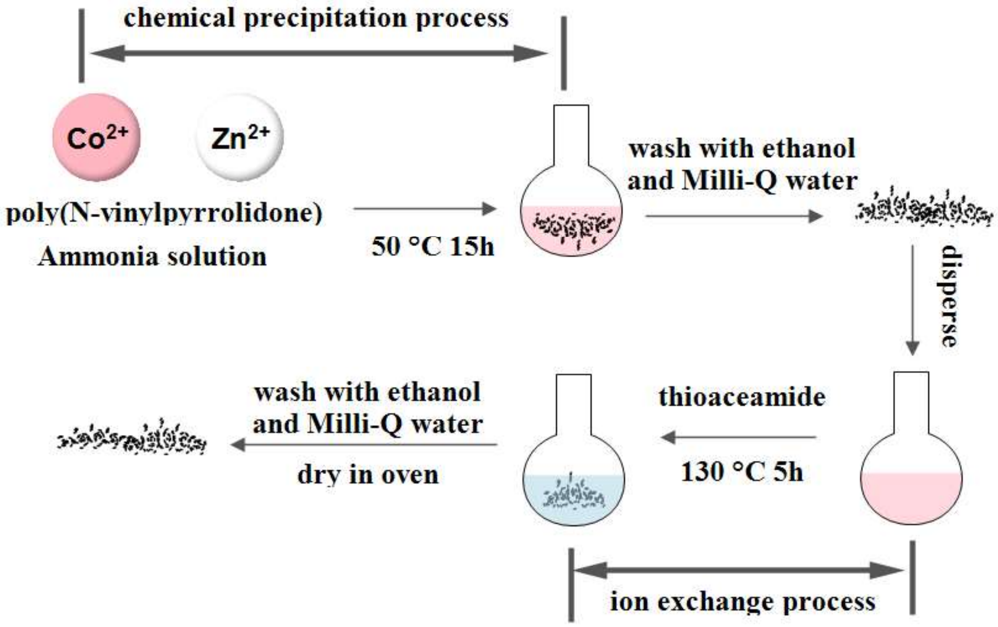

Fig. 1. Illustration of the synthesis route of the Zn: Co (1:2) at 50°C.

2.2.3. Preparation of porous reduced graphene oxide (PrGO)

Firstly, graphene oxide (GO) was prepared using the modified Hummers' method [33]. Porous reduced graphene oxide (PrGO) was synthesized according to the work of Chen *et al.* [34] starting from GO. A homogeneous (25 mL, 2.5 wt.%) GO aqueous solution was prepared by ultrasonication for 30 min. After that, 160 mg $KMnO_4$ were added to the above solution under vigorous stirring. The resulting mixture was kept in a covered beaker for 2 h then 3 mL of HCl and 5 mL of H_2O_2 were added sequentially. The obtained product was collected after reaction for another 3 h, and washed with Milli-Q water. The second step was the reduction of the above product. Here, 1.26 mL (35 wt.%) of ammonia were added to 21 mL (2.3 wt.%) of the above aqueous solution under mechanical stirring; after 60 min, 84 µL of hydrazine were added to the mixture and maintained under mechanical stirring for an additional hour. The mixture was subsequently heated at 90 °C~100 °C under mechanical stirring for 12 h. The formed black precipitate was collected through centrifugation, and rinsed copiously with ethanol and Milli-Q water. The sample was labelled as PrGO. Reduced graphene oxide was also prepared using a similar approach without the pre-oxidation step, and the sample was labelled as rGO.

2.3. Construction of an asymmetric supercapacitor

To further assess the practical usage of the ZnCoS electrode, an asymmetric supercapacitor (ASC) device was fabricated. The ASC device consists of ZnCoS anode, PrGO cathode, and the separator, obtained by soaking a filter paper into 2 M KOH aqueous solution for several minutes. A photograph of the asymmetric supercapacitor test cell with two crocodile clips is depicted in Fig. S1.

The working potential window of the asymmetric supercapacitor was optimized based on the working potential range of ZnCoS and PrGO in a 3-electrode system.

To obtain better ASC performance, the mass ratio of anode and cathode materials was calculated according to the charge balance between the two electrodes. The charge equation can be expressed as follows [35]:

$$\mathrm{q} = \mathrm{C} \times \Delta\mathrm{E} \times \mathrm{m} \qquad (1)$$

Where q is the stored charges in the electrodes, C is the specific capacitance (F g^{-1}), ΔE is the working potential window range (V), and m is the mass of the electrode [36]:

$$\frac{m_+}{m-} = \frac{C_- \times \Delta E_-}{C_+ \times \Delta E_+} \qquad (2)$$

C_- and C_+ are the specific capacitance of cathode and anode, respectively (F g^{-1}), ΔE_- and ΔE_+ are the working potential window range of cathode and anode, respectively (V), m_- and m_+ are the mass of the cathode and anode, respectively.

The energy density (E) and power density (P) are also two important parameters to assess the performance of a supercapacitor. The values of E and P of the fabricated ASC cells were calculated by using the following equations [37]:

$$E = \frac{i \int V(t)dt}{3.6m} \qquad (3)$$

$$P = \frac{E \times 3600}{T_d} \qquad (4)$$

E is the energy density, i is the current, $\int V(t)dt$ is the integral area of the discharging curve, m is the mass of active electrode material, P is the power density, and T_d is the discharge time.

3. Results and discussion

3.1. Characterization of prepared nanomaterials

The chemical composition and oxidation state of surface elements of the synthesized samples were assessed by X-ray photoelectron spectroscopy (XPS). The XPS full spectrum of Zn: Co (1:2) 50 is depicted in Fig. 2a. It comprises peaks attributed to Co, Zn and S, while other elements (C, O, N) due to the stabilizer PVP are also detected.

The Co_{2p} high resolution XPS spectrum of the sample Zn: Co (1:2) 50 consists of $Co_{2p3/2}$ and $Co_{2p1/2}$ spin-orbit doublets and two shakeup satellites (Fig. 2b). The bands at 779.3 and 783.1 eV are assigned to $Co_{2p3/2}$ of Co^{3+} and Co^{2+}, respectively. The bands at binding energies of 794.5 and 798.1 eV are characteristic of $Co_{2p1/2}$ of Co^{3+} and Co^{2+}, respectively. The difference of the binding energy between $Co_{2p1/2}$ and $Co_{2p3/2}$ is larger than 15 eV, revealing the co-existence of Co^{3+} and Co^{2+} in Zn: Co (1:2) 50.

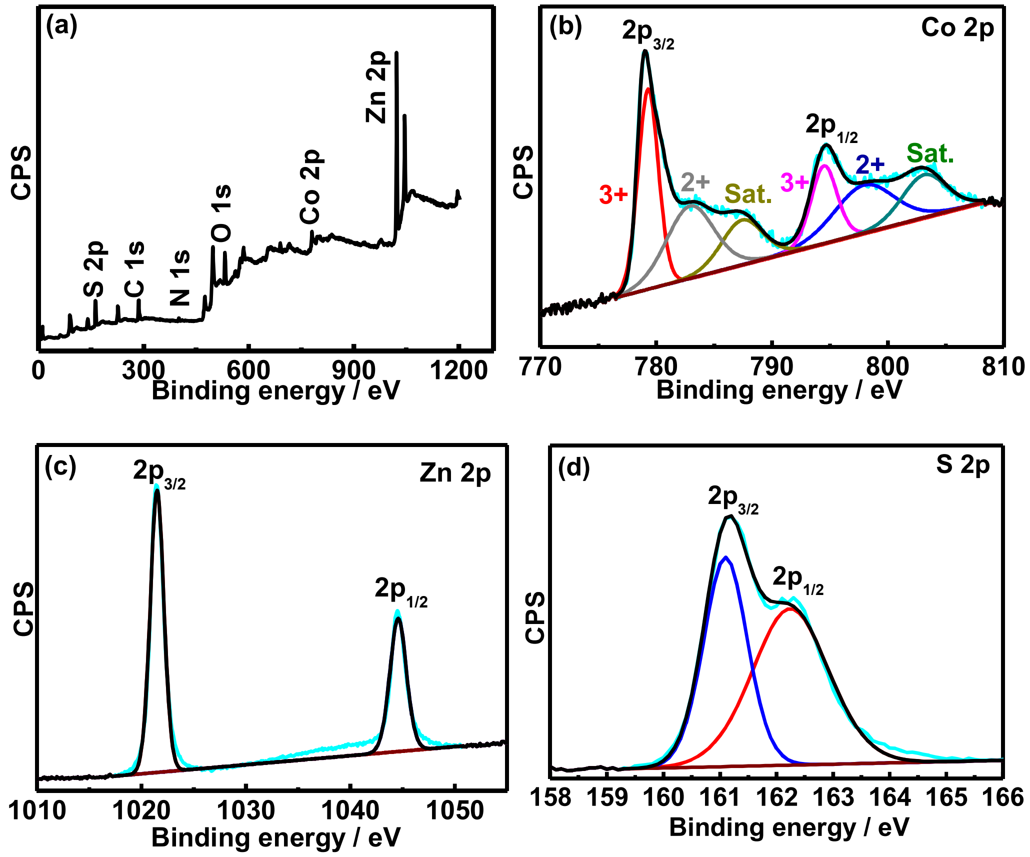

Fig. 2. XPS analysis of Zn: Co (1:2) 50 nanomaterial: (a) full spectrum, (b) high resolution of Co_{2p} (c) Zn_{2p}, (d) S_{2p}. "Sat" in Fig. 2b denotes satellite peaks.

The bands at binding energies of 787.6 and 803.4 eV are the shakeup satellites, in agreement with the literature data for bimetallic sulfides [38-40]. In the XPS high resolution spectrum of Zn_{2p}, two prominent peaks at 1021.5 and 1044.5 eV due to $Zn_{2p3/2}$ and $Zn_{2p1/2}$, respectively are observed, indicating the presence of Zn^{2+} (Fig. 2c) [22-24]. The XPS high resolution spectrum of S_{2p} can be deconvoluted in two bands at 161.1 and 162.2 eV due to $S_{2p3/2}$ and $S_{2p1/2}$, respectively (Fig. 2d). The absence of components at higher binding energies clearly indicates that sulfur is not oxidized. From XPS analysis results, the obtained Zn: Co (1:2) 50 consists of Zn^{2+}, Co^{2+}, Co^{3+}, and S^{2-}. Similar results were obtained for Zn: Co (1:2) RT (Fig. S2).

The crystal structure of the synthesized ZnCoS nanomaterials was determined by XRD technique (Fig. 3). For Zn: Co (1:2) 50 sample, diffraction peaks at 2θ values of 28.6°, 47.8° and 56.7° ascribed to the (111), (220) and (311) crystal planes, respectively can be well indexed to the diffraction patterns of cubic planes of $Zn_{0.76}Co_{0..24}S$ (ZnCoS) (JCPDS card No. 47-1656). XRD patterns of Zn:Co (1:0) RT and Zn:Co (0:1) RT were also given. For Zn: Co (1:0) RT sample, diffraction peaks at 2θ values of 28.6°, 47.6° and 56.4° corresponding to the (111), (220) and (311) crystal planes, respectively can be indexed to the diffraction planes of face centered cubic sphalerite structure of ZnS (JCPDS card No. 05-0566) [22, 41-42]. For Zn: Co (0:1) RT sample, diffraction peaks at 2θ values of 30.8° and 54.8° attributed to the (100) and (110) crystal planes can be indexed to the diffraction planes of CoS (JCPDS card No. 65-3418). In addition, other diffraction peaks between 15.0° and 25.0° indicate the formation of orthorhombic sulfur impurities in the Zn: Co (0:1) RT sample (JCPDS card No. 08-0247). From the XRD results, it could be concluded that the XRD pattern of the Zn:Co (1:2) 50 is very close to that of ZnS sample, except that the diffraction peaks become slightly broader. Therefore, we can hypothesize that during the synthesis, partial substitution of Zn^{2+} by Co^{2+}/Co^{3+} ions in the ZnS lattice took place, instead of the substitution of Co^{2+}/Co^{3+} by Zn^{2+} ion in CoS lattice. Indeed, the size of Zn^{2+} ion (74 pm) is slightly larger than that of Co^{2+} ion (70 pm) or Co^{3+} ion (60 pm); therefore, partial substitution of Zn^{2+} by Co^{2+} or Co^{3+} ions would not significantly affect the cell parameters. Similar XRD patterns were recorded for ZnCoS prepared under different experimental conditions (Fig. S3). Furthermore, the interplanar distance d of obtained sample was calculated according to Bragg's law:

$$2d\sin\theta = n\lambda \qquad (5)$$

Where θ is the scattering angle, d is the interplanar distance, n is a positive integer and λ=1.54056 Å.

The interplanar distance d of diffraction peaks 2θ at values of about 28.6°, 47.8° and 56.7° corresponds to ~0.30, 0.19 and 0.16 nm, respectively.

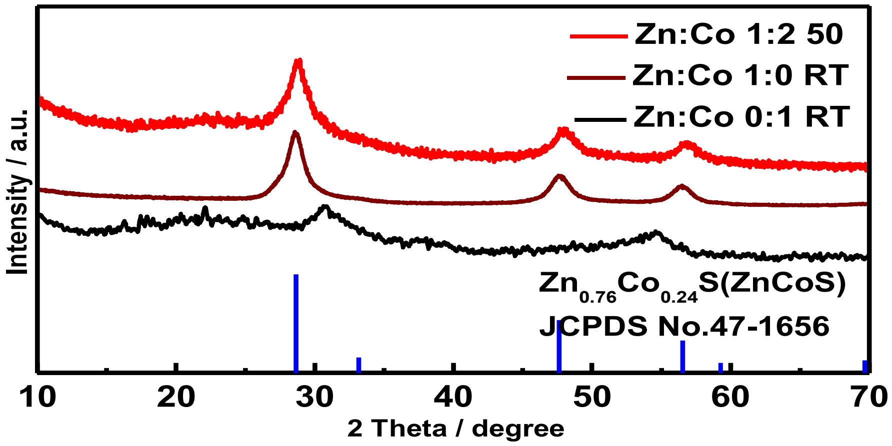

Fig. 3. XRD patterns of the prepared ZnCoS materials.

The particle size of ZnCoS sample can be determined by using the Debye-Scherrer formula [23]:

$$D = \frac{0.94\lambda}{\beta Cos\theta} \qquad (6)$$

Where β is the full width at half maximum intensity and λ = 1.54056 Å.

Based on the full width at half maximum (FWHM) of diffracted peaks of sample Zn: Co (1:2) 50, the calculated average particle size was 5 nm using (1 1 1) peaks.

The existence of Co and Zn in prepared ZnCoS samples was confirmed by ICP-AES analysis (Table 2). The influence of initial mole ratio of Co/Zn and temperature during the chemical precipitation process on final ratio of Co/Zn (wt.%/wt.%) of ZnCoS were also investigated. When the temperature during the chemical precipitation process was fixed, the amount of Co in prepared ZnCoS samples increased from 22.66 to 31.73% when the initial mole ratio of Co/Zn increases, and the final ratio of Co/Zn (wt.%/wt.%) increases as well from 0.45 to 0.73. When the initial mole ratio of Co/Zn is fixed, the final ratio of Co/Zn (wt.%/wt.%) increases from 0.55 to 1.25 upon increasing the temperature from room temperature (RT) to 80°C, indicating that much more Zn^{2+} ions were replaced by Co^{2+}/Co^{3+} ions as the chemical precipitation temperature was increased. It is worth noticing that the final ratio of Co/Zn (wt.%/wt.%) of ZnCoS sample, synthesized at higher chemical precipitation temperature, is significantly larger than that prepared at room temperature. Therefore, improving the chemical precipitation temperature was believed to be much more effective to obtain a much higher ratio of Co/Zn (wt.%/wt.%) in ZnCoS lattice. Furthermore, according to the ICP-AES results, the exact chemical composition of the samples was deduced.

Table 2. Co and Zn composition obtained by ICP-AES analysis.

Sample	Zn (wt.%)	Co (wt.%)	Co/Zn (wt.%/wt.%)	Formula
Zn: Co (1:1) RT	50.80	22.66	0.45	$Zn_{0.70}Co_{0.30}S$
Zn: Co (1:2) RT	45.72	25.36	0.55	$Zn_{0.65}Co_{0.35}S$
Zn: Co (1:3) RT	43.40	31.73	0.73	$Zn_{0.58}Co_{0.42}S$
Zn: Co (1:2) 50	37.62	43.54	1.16	$Zn_{0.46}Co_{0.54}S$
Zn: Co (1:2) 80	29.68	36.97	1.25	$Zn_{0.45}Co_{0.55}S$

The morphology and detailed microstructures of the prepared ZnCoS nanoparticles were examined by transmission electron microscopy (TEM) and scanning electron microscopy (SEM). The TEM image of Zn: Co (1:2) 50 nanoparticles exhibits a quasi-sheet-like structure (Fig. 4a). The selected area electron diffraction (SAED) image displays rings and dots, which are indicative of the crystalline nature of the nanoparticles (Fig. 4b). The calculated interplanar distance d values from SAED are ~0.30, 0.19 and 0.16 nm, agreeing well with the distance of the (1 1 1), (2 2 0) and (3 3 3) crystal planes, respectively of obtained Zn: Co (1:2) 50 sample (Fig. 3). From the HRTEM images in Fig. 4c, d, the lattice fringes of 0.19 nm (Fig. 4c) and 0.30 nm (Fig. 4d) also match well with the interplanar distance d calculated from the XRD pattern of Zn: Co (1:2) 50 sample (Fig. 3). The results are in accordance with the XRD measurements. The high resolution TEM image in Fig. 4c also suggests that the sheet-like structure is made up of several nanoparticles. The low magnification SEM images of Zn: Co (1:2) 50 sample (Fig. 4e, f) reveal that its surface is very rough and has a porous structure, which is expected to provide more electroactive sites between the active material and the electrolyte.

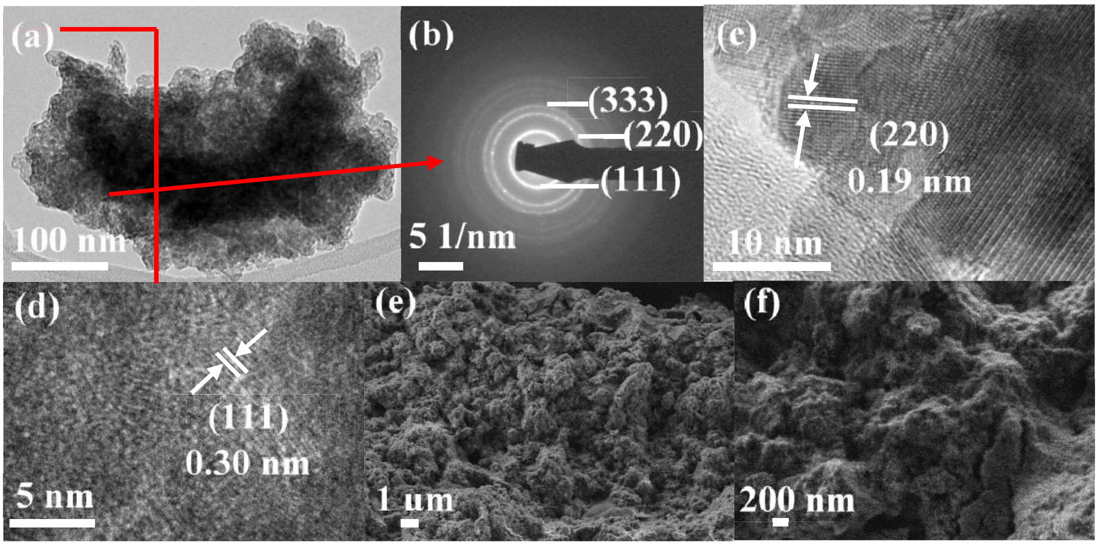

Fig. 4. TEM images (a), SAED pattern (b), HRTEM images (c, d), and SEM images (e, f) of Zn:Co (1:2) 50 sample.

The specific surface area (SSA) and porous texture of obtained ZnCoS samples were examined by nitrogen adsorption-desorption isotherms (Fig. 5). The nitrogen adsorption-desorption isotherms of ZnCoS samples was identified as type IV according to the IUPAC (International Union of Pure and Applied Chemistry) classification. Also hysteresis loops in the 0.5-0.9 relative pressure region were observed (Fig. 5a), suggesting the existence of mesoporous structures, which were further investigated in the pore diameter distribution profile (Fig. 5b), determined from the desorption isotherm using the BJH model. The pore diameter peak observed at around 6, 6 and 10 nm also proves the presence of a mesoporous structure in the Zn: Co (1:2) RT, Zn: Co (1:2) 50, Zn: Co (1:2) 80 samples, respectively. The BET SSA of Zn: Co (1:2) 50 is 112.4 $m^2 g^{-1}$, much higher than that of Zn: Co (1:2) RT (76.6 $m^2 g^{-1}$) and Zn: Co (1:2) 80 (62.2 $m^2 g^{-1}$) samples. This confirms that the temperature during the chemical precipitation process has an influence on the SSA value and the sample prepared at 50°C offered the highest SSA value. This value is larger than that reported for metal sulfides such as hollow ellipsoid Ni-Mn sulfides (48.1 $m^2 g^{-1}$) [43], $NiCo_2S_4$ (42.8 $m^2 g^{-1}$) [44], $ZnS/NiCo_2S_4/Co_9S_8$ (28.1 $m^2 g^{-1}$) [45] and $CuCo_2S_4$ nanoparticles (12.2 $m^2 g^{-1}$) [46].

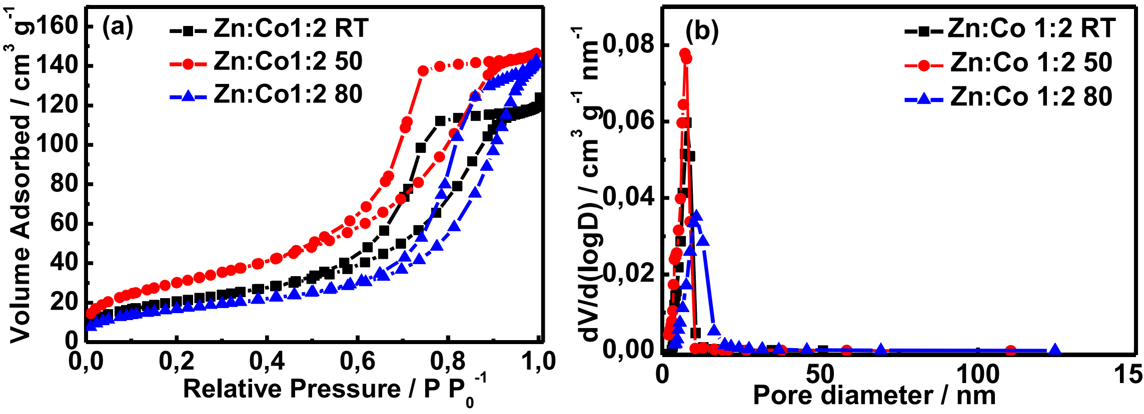

Fig. 5. Nitrogen adsorption/desorption isotherms (a), and pore size distribution curves (b) of ZnCoS samples.

3.2. Electrochemical properties

3.2.1. Cathode materials

Two electrode materials, namely reduced graphene oxide (rGO) and porous reduced graphene oxide (PrGO), were investigated as cathodes through their electrochemical performance in 2 M KOH aqueous solution (Fig. 6). No obvious oxidation/reduction peaks could be seen in the investigated voltage region (Fig. 6a), suggesting that energy storage takes place mainly through double-layer capacitance. PrGO electrode displays a much larger integrated area, indicating that PrGO electrode exhibits an enhanced electrochemical activity. From the GCD curves (Fig. 6b), we can see that the charge and discharge curves display a triangle-like shape, proving the absence of a redox pseudocapacitive behavior; the PrGO electrode offers a much longer charging and discharging time (940 s at 0.5 A g^{-1}) than that of rGO electrode (200 s at 0.5 A g^{-1}). Using equations S(1) and S(2), the specific capacitance of both electrodes was calculated from Fig. S4. The trend of the specific capacitance values, determined from GCD curves, matches well with the result deduced from the CV curves, and the electrode PrGO provided a much higher specific capacitance value (270.8 F g^{-1} at 0.5 A g^{-1}), compared to that of rGO electrode (62.4 F g^{-1} at 0.5 A g^{-1}), Fig. S5 and Fig. 6c. The results reveal that the oxidation process of GO followed by reduction with ammonia and hydrazine enhances the electrochemical activity of rGO. Fig. 6d displays the Nyquist plots of rGO and PrGO electrodes along with the equivalent circuit (Inset). In the equivalent circuit, the symbols R_s, C_{dl}, R_{ct}, and W and C_l denote the series resistance, capacitance of double layer, charge-transfer resistance, Warburg impedance, and the limit capacitance, respectively [47]. As can be seen, the electrode PrGO has a lower R_s (~1.12 ohm·cm^2) than the electrode rGO

(~1.85 ohm·cm^2), suggesting the porous structure could reduce the series resistance effectively. The PrGO electrode also has a much smaller R_{ct} (~2.53 ohm·cm^2) than that of rGO electrode (~496.81 ohm·cm^2), indicating a faster charge transfer speed during the electrochemical process. The enhanced electrochemical activity is assigned to the unique porous structure of PrGO, as evidenced by the TEM image in Fig. S6. This porous structure is expected to allow convenient pathways for the transportation of ions and electrons between the electrolyte and active material, and provide efficient and fast ion diffusion.

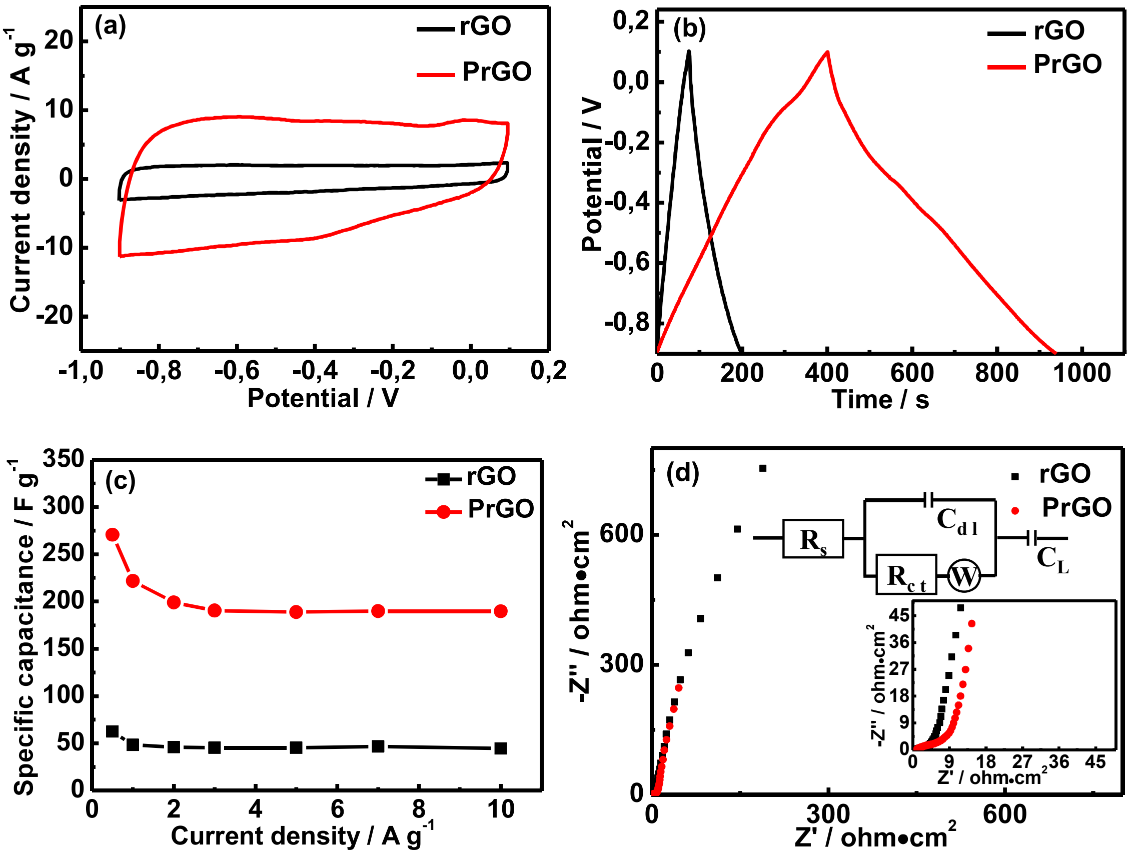

Fig. 6. Electrochemical properties of rGO and PrGO in 2 M KOH: (a) CV curves at a scan rate of 50 mV s^{-1} in the potential range of -0.9 to +0.1 V; (b) GCD curves at a current density of 0.5 A g^{-1} in the potential range of -0.9 to +0.1 V; (c) the corresponding specific capacitance values at different current densities (0.5-10 A g^{-1}); (d) The Nyquist plots. The inset in (d) is the corresponding equivalent circuit.

3.2.2. Anode materials

The CV and GCD curves of Zn: Co (1:0) RT electrode were depicted in Fig. S7a, b, where a pair of oxidation and reduction peaks could be seen within the 0 to +0.55 V potential range (Fig. S7a), which is believed to be caused by the reversible faradaic redox reaction of Zn-S-

OH. The charge-discharge curves comprise two potential plateaus, which match well with the CV results (Fig. S7b).

Next, the influence of the initial mole ratio of Co/Zn and temperature during the chemical precipitation process on the electrochemical properties of ZnCoS were examined. Fig. 7 depicts the electrochemical behavior of the synthesized electrodes through CV and GCD characterization. As previously, both oxidation and reduction peaks are present in all CV curves of ZnCoS electrodes, prepared under different experimental conditions (Fig. 7a), indicating battery-type characteristics of the ZnCoS materials [48].

By increasing the initial mole ratio of Co/Zn (1:1, 2:1, 3:1) while the temperature of the precipitation reaction was kept at room temperature, the 2:1 ratio provided the largest current density. Next, the effect of temperature (RT, 50, 80°C) during the chemical precipitation process on electrochemical performance of ZnCoS (Co: Zn = 2:1) was assessed. The results clearly demonstrate that the ZnCoS sample prepared at 50°C achieved the largest current density, suggesting that the most suitable temperature during the chemical precipitation process is 50°C.

Furthermore, CV curves of Zn: Co (1:0) RT, Zn: Co (1:2) 50, and Zn: Co (0:1) RT electrodes and bare nickel foam at the scan rate of 10 mV s^{-1} in the potential range of 0 to +0.55 V were also depicted in Fig. S8. The redox peaks observed in the CV curve of Zn: Co (0:1) RT electrode, according to the literature reports [49-50], are likely due to the oxidation of CoS to CoSOH and CoSOH to CoSO, respectively. The redox peaks in the CV curve of Zn: Co (1:0) RT are believed to be caused by the reversible faradaic redox reaction of Zn-S-OH. Therefore, the increase of current density and redox peaks seen in the CV curve of Zn: Co (1:2) 50 electrode is attributed to the following faradaic redox reactions:

$$ZnS + OH^- \rightarrow ZnSOH + e^-$$

$$CoS + OH^- \rightarrow CoSOH + e^-$$

$$CoSOH + OH^- \rightarrow CoSO + H_2O + e^-$$

Two potential plateaus are apparent in the charge-discharge curves (Fig. 7b), which match well with the CV results. These potential plateaus confirm the existence of faradaic redox reaction behavior and the characteristics of battery-type capacitance. The discharge time also gives an indication on the specific capacitance; a longer discharge time implies a larger specific capacitance. The GCD results reveal that the electrode Zn: Co (1:2) RT (220 s) exhibits a much longer time than the Zn: Co (1:0) RT (87 s), Zn: Co (1:1) RT (125 s), Zn: Co (1:3) RT (189 s), and Zn: Co (0:1) RT (143 s) electrodes, indicating 2 is the best initial mole ratio between Co and Zn. The electrode Zn: Co (1:2) 50 displays the longest discharge time, as compared with the Zn: Co (1:2) RT and Zn: Co (1:2) 80 electrodes, suggesting that the Zn: Co (1:2) 50 electrode could provide the largest charge storage ability. The results from GCD curves analysis are consistent with the results of CV curves above. We can conclude that the sample synthesized at 50°C using an initial mole ratio Co/Zn = 2 provides the highest specific capacitance.

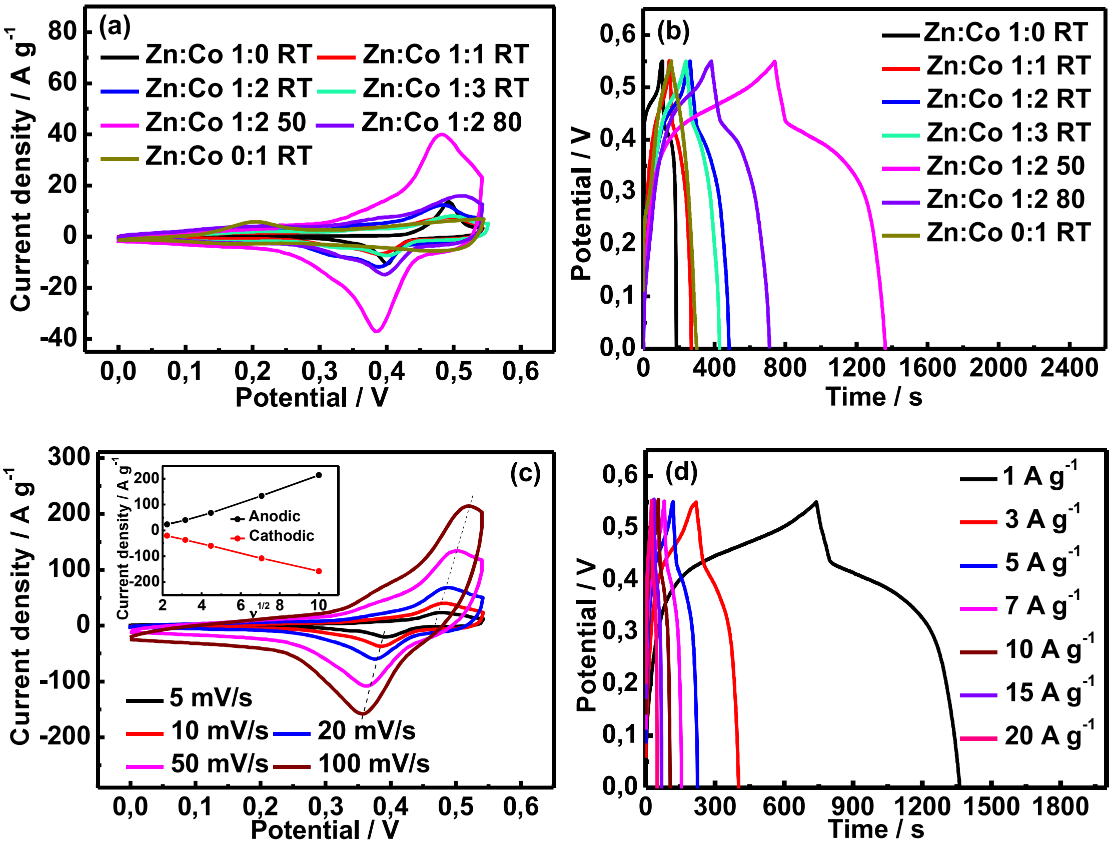

Fig. 7. Electrochemical properties of ZnCoS nanoparticles in 2 M KOH in the 0 - +0.55 V potential range: (a) CV curves of all electrodes recorded at a scan rate of 10 mV s^{-1}; (b) GCD curves of all electrodes recorded at a current density of 1 A g^{-1}; (c) CV curves of Zn: Co (1:2) 50 electrode recorded at a scan rate of 5 -100 mV s^{-1}; (d) GCD curves measured at a current density of 1, 3, 5, 7, 10, 15 and 20 A g^{-1}; the inset in (c) is the anodic and cathodic peak current density as a function of the square root of sweep rate.

Furthermore, CV and GCD curves of the Zn: Co (1:2) 50 electrode at different sweep rates and current densities are shown in Fig. 7c, d. As the sweep rate increases (Fig. 7c), the current density response enhances as well, while the general shape of the CV curves is not altered, indicating that the electrode exhibits a good rate capability. Moreover, a small shift of about

40 mV could be observed when the sweep rate increases from 5 to 100 mV s^{-1}, suggesting that the prepared electrode possesses low polarization [51-53]. The inset of Fig. 7c depicts the anodic and cathodic peak current densities as a function of the square root of sweep rate. The well fitted linear relationship reveals that the redox reactions of the electrode are controlled by the diffusion of OH^- [53]. Fig. 7d shows the GCD curves of the same electrode at a current density of 1, 3, 5, 7, 10, 15 and 20 A g^{-1} (potential range: 0 to +0.55 V). The obvious potential plateaus observed in the GCD curves nicely agree with the redox behavior recorded in the CV curves, revealing strong pseudocapacitive behavior.

Using equations S(1) or S(2), specific capacitance values determined from the CV curves or the time for discharging process in GCD curves (Fig. 7a, b) are summarized in Table 3. The trend of specific capacitance values, estimated from the GCD curves, matches well the results deduced from the CV curves. Zn: Co (1:2) 50 electrode offers the highest specific capacitance value.

Table 3. Specific capacitance of ZnS and ZnCoS nanoparticles.

Sample	Specific capacitance (F/g) in 2 M KOH electrolyte	
	Galvanostatic discharge (1 A g^{-1})	CV (10 mV s^{-1})
Zn: Co (1:0) RT	148.1	135.4
Zn: Co (1:1) RT	227.4	220.8
Zn: Co (1:2) RT	400.5	373.4
Zn: Co (1:3) RT	344.8	269.4
Zn: Co (1:2) 50	1134.7	986.8
Zn: Co (1:2) 80	562.0	481.7
Zn: Co (0:1) RT	260.5	320.6

The CV and GCD curves of ZnCoS electrodes, prepared under different experimental conditions, were also recorded, and the corresponding CV curves and GCD curves measured at different sweep rates and current densities were displayed in Fig. S7c-o. Here, redox peaks and potential plateaus are also detected in all CV and GCD curves, respectively. However, the maximum current density and time for charge and discharge at the same condition are smaller than those of the Zn: Co (1:2) 50 electrode. The specific capacitance values, calculated according to these curves, are exhibited in Fig. 8a, b. The electrode Zn: Co (1:2) 50 offers the largest specific capacitance. In Fig. 8a, one clearly sees that when the scan rate increases, the specific capacitance of the ZnCoS electrodes decreases. This is most likely due to reduced effective interaction between the electrode surface and OH^- ions at higher scan rates [54]. The Zn: Co (1:2) 50 electrode achieves specific capacitance values of 1029.8, 986.8, 871.3, 713, 558.2 F g^{-1} at 5, 10, 20, 50, 100 mV s^{-1}, respectively, which are much higher than those determined for other ZnCoS electrodes and is 5.3 times larger than that of Zn: Co (1:0) RT nanoparticles (194.9 F g^{-1} at 5 mV s^{-1}) and 3.0 times larger than that of Zn: Co (0:1) RT (344.5 F g^{-1} at 5 mV s^{-1}). As shown in Fig. 8b, the Zn: Co (1:2) 50 electrode offers a specific capacitance of 1134.7, 1011.1, 971.7, 961.9, 949.5, 931.9, 919.6 F g^{-1} at 1, 3, 5, 7, 10, 15, 20 A g^{-1}, respectively. As the current density increases from 1 A g^{-1} to 20 A g^{-1}, 81% of the initial specific capacitance is preserved even at 20 A g^{-1}, highlighting a good rate capability of the Zn: Co (1:2) 50 electrode. This electrode offers a maximum specific capacitance of 1134.7 F g^{-1} at 1 A g^{-1}, which is about 7.7 times than that of Zn: Co (1:0) RT nanoparticles (148.1 F g^{-1} at 1 A g^{-1}) and 4.4 times than that of Zn: Co (0:1) RT nanoparticles (260.5 F g^{-1} at 1 A g^{-1}). Moreover, using the same temperature during the chemical precipitation process, the Zn: Co (1:2) RT exhibits larger specific capacitance compared to electrodes prepared using a Co/Zn mole ratio of 0:1, 1:1, 3:1, indicating that the Co/Zn ratio has a significant influence on the electrochemical properties. Using the same initial mole ratio of Co/Zn (2:1), the Zn: Co (1:2) 50 also displays a larger specific capacitance compared to that of samples prepared at RT and 80 °C, indicating that the temperature also has a pronounced effect on the electrochemical properties.

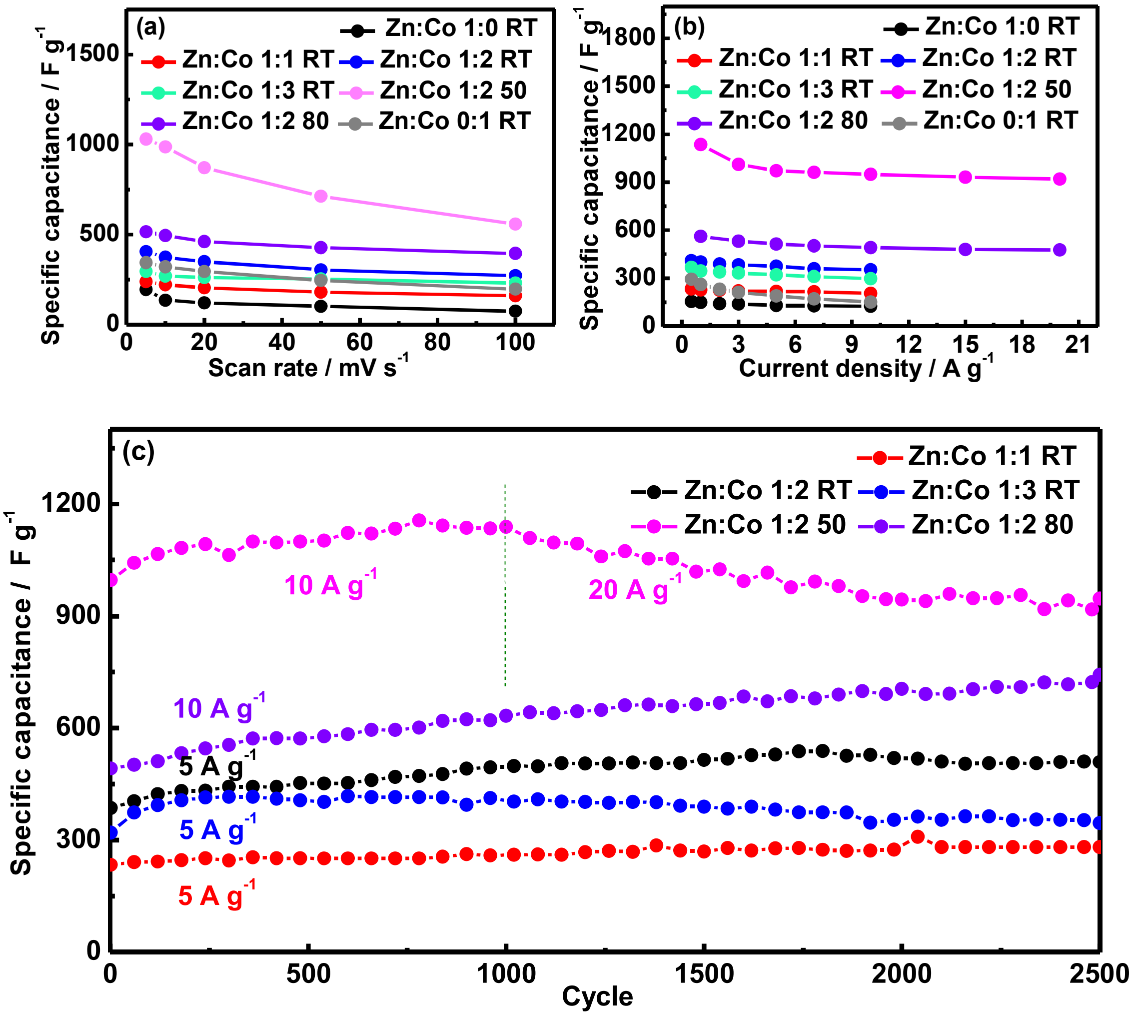

Fig. 8. (a) Specific capacitance at sweep rates of 5-100 mV s^{-1} and (b) at current densities of 0.5-20 A g^{-1}; (c) Cycling performance of ZnCoS electrodes for 2500 charge/discharge cycles.

The cycling stability of ZnCoS electrodes was also examined by repeated charge/discharge cycles at different current densities for 2500 cycles. The data in Fig. 8c revealed that the ZnCoS electrodes, prepared using a precipitation process at RT, achieve specific capacity retention of 120%, 132%, 108% for Zn: Co (1:1), Zn: Co (1:2), Zn: Co (1:3), respectively after 2500 cycles at 5 A g^{-1}, indicating a good cycling stability.

In comparison, the stability of the Zn: Co (1:2) 50 electrode was tested at different current densities using the following sequence: 10 A g^{-1} for the first 1000 cycles and 20 A g^{-1} for additional 1500 cycles. A retention of ~115% is obtained at 10 A g^{-1}, which slightly drops to 103% at 20 A g^{-1}. According to the cycling performance examination, even after 2500 cycling, the Zn: Co (1:2) 50 electrode still offers the highest specific capacitance (946.3 F g^{-1}

at 20 A g^{-1}). Zn: Co (1:2) 80 electrode retains ~150% of its initial capacitance value after 2500 charge-discharge cycles at 10 A g^{-1}.

Moreover, the specific capacitance of synthesized Zn: Co (1:2) 50 electrode is also superior to those previously reported ZnCoS electrode materials (Table S1). Such a desirable performance of prepared Zn: Co (1:2) 50 electrode indicates the potential usage for energy storage devices.

Fig. 9 compares the electrochemical properties of Zn: Co (1:2) 50 electrode before and after the stability test in the same electrolyte (2 M KOH). After 2500 cycles, the redox peaks in the CV curves are enhanced (Fig. 9a), while in the GCD curves longer charging and discharging times are observed at a current density of 5 A g^{-1} (Fig. 9b). Given that the time for discharging process affects the capacity ability of electrode materials, a longer discharging time indicates a much larger specific capacity. From the results, it can be concluded that a much larger specific capacity was reached after 2500 cycles. A small difference in the R_s values (~0.92 ohm·cm^2 after the 1st cycle and ~1.11 ohm·cm^2 after 2500th cycle) is observed in 2 M KOH aqueous solution (Fig. 9c). Nyquist plots of other ZnCoS electrodes are also displayed in Fig. S9a, along with the corresponding equivalent circuit. In the equivalent circuit, the symbols R_s, CPE, R_{ct}, and W and C_l denote the series resistance, Constant Phase Element, charge-transfer resistance, Warburg impedance, and the limit capacitance, respectively. The R_s and R_{ct} values, calculated according to the equivalent circuit in the inset, are summarized in Table S2. Here, ZnCoS electrode materials, prepared at higher temperature, offer a much smaller charge transfer resistance, suggesting that ZnCoS prepared at higher temperature could provide a faster electron transfer speed during the electrochemical process.

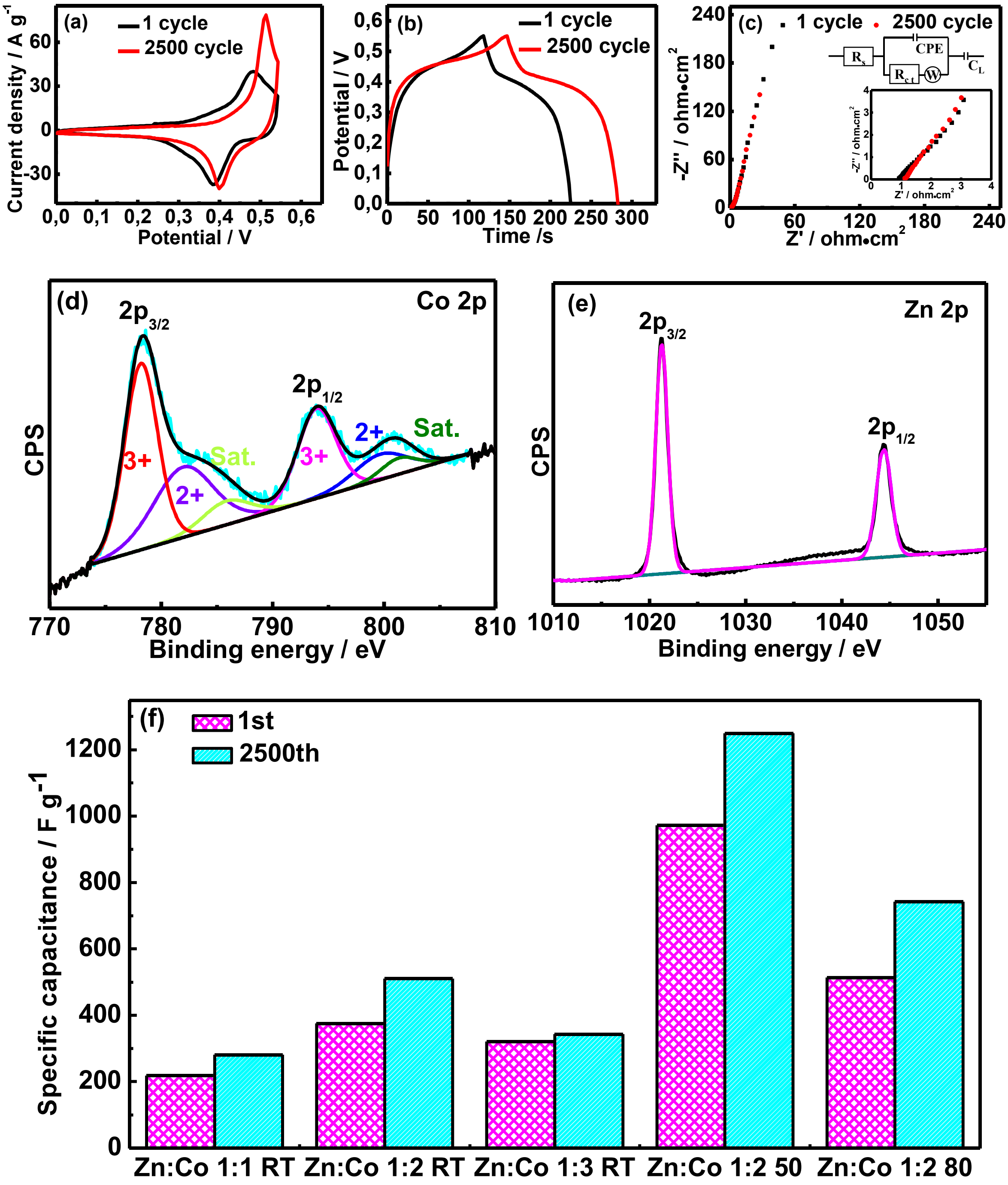

Fig. 9. (a) CV curves after the first and 2500th cycle at a scan rate of 10 mV s^{-1} (potential range: 0 to +0.55V); (b) GCD curves after the first and 2500th cycle recorded at a current density of 5 A g^{-1}, (c) Nyquist plots after the first and 2500th cycle (the inset is the corresponding equivalent circuit), (d, e) high resolution XPS spectra of the Co$_{2p}$ and Zn$_{2p}$ after the cycling test for 2500th cycles of Zn: Co (1:2) 50, (f) Specific capacitance of all ZnCoS electrodes before and after stability test at a current density of 5 A g^{-1} in 2 M KOH aqueous solution. “Sat” in Fig. 9d denotes satellite peaks.

Furthermore, the chemical composition of the electrode material after the cycling stability test was examined by XPS. Fig. 9d, e depicts the XPS high resolution spectrum of the Co_{2p} and Zn_{2p} of Zn: Co (1:2) 50 after 2500 cycles, respectively. The XPS spectrum of Co_{2p} can be fitted with two spin-orbit peaks at 779.0 and 794.7 eV attributed to $Co^{3+}{}_{2p3/2}$ and $Co^{3+}{}_{2p1/2}$, respectively. Another two broadened peaks (at ~783.7 and 800.9 eV) ascribed to $Co^{2+}{}_{2p3/2}$ (at ~782.8 eV), $Co^{2+}{}_{2p1/2}$ (at ~800.5 eV), and two satellite peaks (at ~786.6 and 802.1 eV) are also evident in the spectrum. The decrease of the intensity of the Co^{2+} (Fig. 9d), compared with the XPS high resolution spectrum of the Co_{2p} of Zn: Co (1:2) 50 (Fig. 2b), suggests ~~the~~ electrochemical transformation of Co^{2+}/Co^{3+} during the supercapacitor operation (charge/discharge cycling). In the XPS spectrum of Zn_{2p} (Fig. 9e), two prominent peaks at 1021.3 and 1044.4 eV due to $Zn_{2p3/2}$ and $Zn_{2p1/2}$, respectively are observed, indicating the presence of Zn^{2+}.

The electrochemical characteristics of the other ZnCoS electrodes before and after the stability test are displayed in Fig. S9b. The specific capacitance values before and after the stability test were calculated from the GCD curves (Fig. 9b, Fig. S9b) and displayed in Fig. 9e. The results revealed that the specific capacitance of all electrodes, deduced from the discharge curves, increased after 2500 cycles. Zn: Co (1:2) 50 electrode offers the highest specific capacitance of 1248.7 F g^{-1} after 2500th cycle at 5 A g^{-1} (971.7 F g^{-1} for 1st cycle).

Furthermore, the stability of the Zn: Co (1:2) 50 electrode was examined at 20 A g^{-1} for 6000 cycles (Fig. 10). It should be noticed that in the first 500 cycles, the specific capacitance value increased from 919.6 F g^{-1} to 1097.8 F g^{-1}, most likely due to the complete activation of the electrode material. After 6000 cycles, the electrode achieved a specific capacitance of 913.9 F g^{-1}, indicating a good cycling stability.

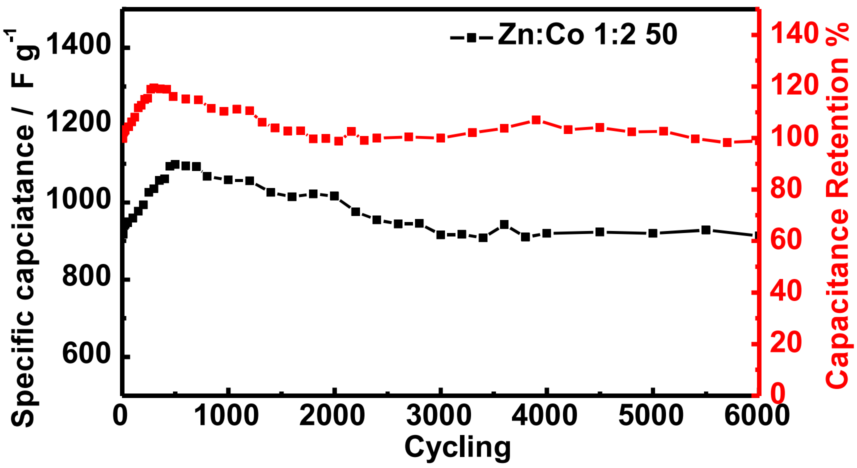

Fig. 10. Cycling performance of Zn: Co (1:2) 50 electrode at 20 A g^{-1} for 6000 cycles.

3.2.3. Fabrication of an asymmetric supercapacitor

To further assess the practical usage of the prepared Zn: Co (1:2) 50 electrode (referred as ZnCoS), an asymmetric supercapacitor (ASC) device was fabricated using ZnCoS anode and PrGO cathode (Fig. 11a). The working potential window of the ASC was determined on the basis of the working potential windows of ZnCoS and PrGO, in a 3-electrode system. Fig. 11b displays the working potential window of PrGO (-0.9 ~ +0.1 V vs. Hg/HgO) and ZnCoS (0 ~ +0.55 V vs. Hg/HgO) electrode at a scan rate of 10 mV s^{-1}. According to the individual electrode potential range, the cell voltage of fabricated ASC is fixed at 1.5 V.

In order to investigate the operating voltage window, a series of CV curves of the assembled ASC at different cell voltages are recorded at 50 mV s^{-1} (Fig. 11c). Interestingly, increasing the cell voltage does not alter the shape of the CV curves, showing the redox peaks within the potential window. The GCD curves at various cell voltage values (current density = 3 A g^{-1}) are also depicted in Fig. 11d. Both CV and GCD curves reveal that the operating potential window for ZnCoS//PrGO asymmetric supercapacitor could be extended to 1.6 V even though 1.5 V is chosen as the cell voltage for further characterization of the electrochemical properties of the device.

Fig. 11e displays the CV curves of the ASC (cell voltage = 1.5 V) as a function of the scan rate (10 - 75 mV s^{-1}). No obvious change in the shape of the CV curves is observed. The variation of the specific capacitance, determined from the CV curves, is depicted in Fig. 11f. The flexible ASC device achieves a maximum specific capacitance of 90 F g^{-1} at a scan rate of 10 mV s^{-1}. The energy density (E) and power density (P) were also determined from the

GCD curves of the ASC device, Fig. S10a. The Ragone plot relating E and P is displayed in Fig. 11g. The fabricated flexible ASC cell exhibits high energy and power densities of about 17.7 W h kg^{-1} and 435 W kg^{-1} at 0.5 A g^{-1}, respectively. The ASC achieves high energy density (13.2 W h kg^{-1}) and power density (11699 W h kg^{-1}) even at a high current density (10 A g^{-1}). This result reveals improved energy density at high power density as compared with other supercapacitor devices (NiS_x//AC, 53.5 W kg^{-1} and 4.1 W h kg^{-1} [18]; MCS/GNF//AC, 74.87 W kg^{-1} and 14.33 W h kg^{-1} [30]; NiS//NiS 250 W kg^{-1} and 16.5 W h kg^{-1} [55]; CoS//CoS, 150 W kg^{-1} and 4.8 W h kg^{-1} [56]; $CuSbS_2$//$CuSbS_2$, 341 W kg^{-1} and 2.6 W h kg^{-1} [57]; $NiCo_2S_4$//C, 160 W kg^{-1} and 22.8 W h kg^{-1}) [58]. Fig. S10b presents the Nyquist plots of the ZnCoS//PrGO ASC device. The internal resistance of the fabricated ASC device is determined to be ~0.2 ohm, while the R_{ct} value due to the charge-transfer resistance is ~24.1 ohm·cm^2.

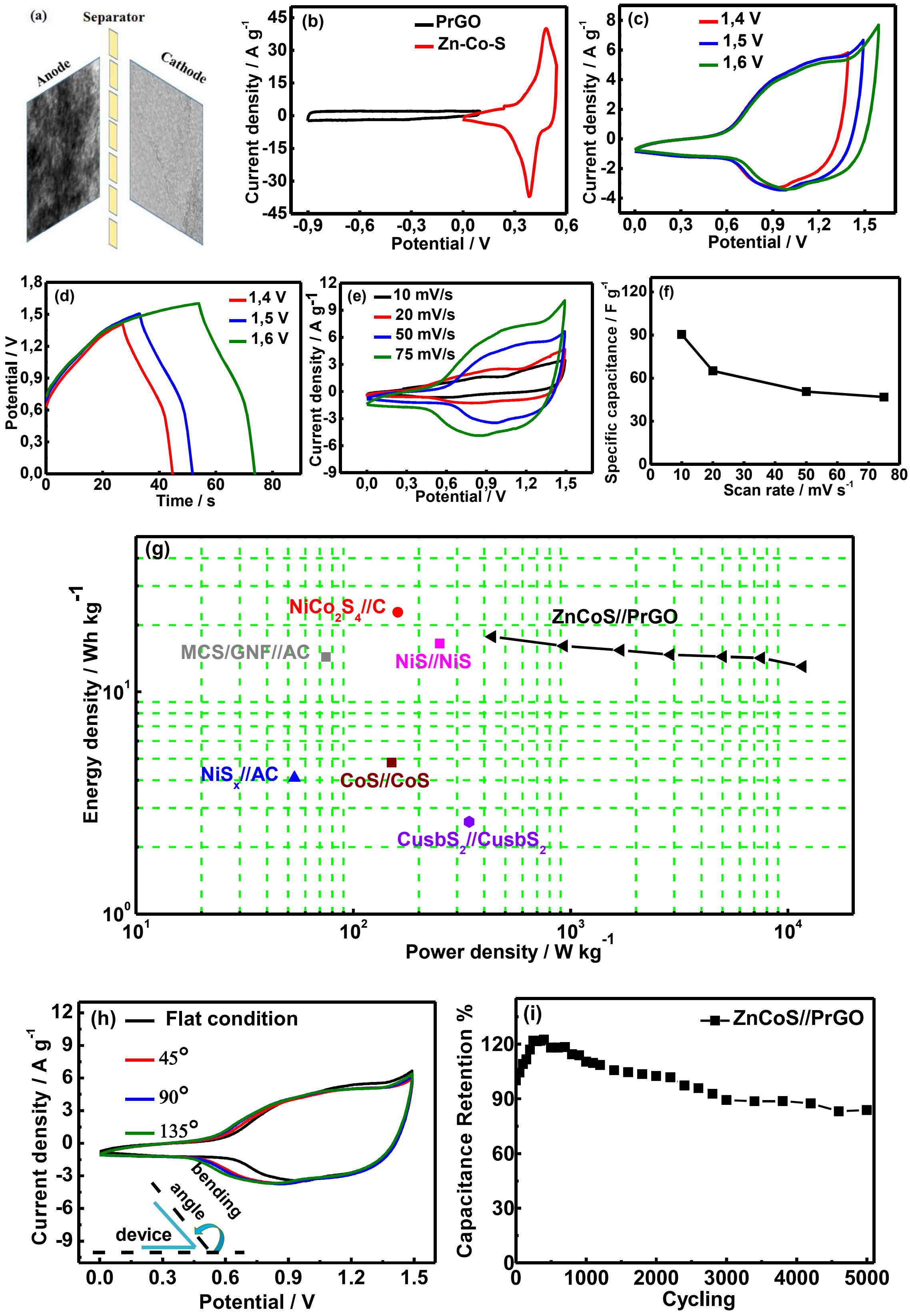

Fig. 11. (a) Schematic diagram of asymmetric ZnCoS//PrGO supercapacitor cell, (b) CV curves of PrGO and ZnCoS electrodes, scan rate=10 mV s^{-1}, (c) CV curves and (d) GCD curves measured at different cell voltage values, (e) CV curves recorded at various scan rates, (f) variation of the specific capacitance *vs.* scan rate, (g) typical Ragone plot of the flexible

ASC device, (h) CV curves of the ASC recorded at 50 mV s^{-1} under different bending angles of 0-135° in 2 M KOH aqueous solution; the inset is the schematic illustration of bent cells, (i) cycling performance of fabricated ASC device at 2 A g^{-1} for 5000 cycles.

In addition, the performance of the ASC device under mechanical strain was examined by recording the CV curves at different bending angles. Fig.11h depicts the CV curves of the ASC device as a function of the bending angle (0 to 135°) recorded at a cell voltage of 1.5 V and a scan rate of 50 mV s^{-1}. No significant distortion of the CV curves was apparent even when the bending angle is as high as 135°, which confirms the good flexibility of the fabricated ASC cell. Furthermore, the stability of the fabricated ASC device was examined at 2 A g^{-1} for 5000 cycles (Fig. 11i). It should be noticed that in the first 400 cycles, the capacitance retention was about 122%, most likely due to the complete activation of both electrode materials. After 5000 cycles, the capacitance retention rate of the prepared ASC device was about 84%, indicating the good cycling stability of the fabricated ASC device.

4. Conclusion

In summary, a series of ZnCoS nanomaterials were synthesized by controlling the initial mole ratio of Co/Zn and the temperature during the chemical precipitation process. Under optimized conditions, the ZnCoS electrode exhibits a specific capacitance of 1134.7 F g^{-1} at 1 A g^{-1}, with good rate capability (81% retention from 1 to 20 A g^{-1}) and excellent cycling stability (almost no obvious decrease of the capacitance at 20 A g^{-1} after 6000 cycles) in 2 M KOH aqueous electrolyte. In addition, ZnCoS electrode displays an improved electrochemical performance than bare ZnS electrode. Furthermore, a ZnCoS//PrGO asymmetric supercapacitor (ASC) was assembled. The device demonstrates a good electrochemical performance within a potential window of 1.5 V along with good energy and power densities. Moreover, no significant distortion of CV curves at different bending angles indicates the good flexibility of the fabricated ASC cell. The results obtained in the present work suggests that ZnCoS can be applied as an anode electrode material for designing flexible supercapacitors with high performance.

Acknowledgement

SS and RB acknowledge financial support from the Centre National de la Recherche Scientifique (CNRS), the University of Lille, and the Hauts-de-France region. N.C. acknowledges support from National Natural Science Foundation of China (grants

No.51701240), Key Research and Development Program of Shandong Province (grant No.2017GGX20123) and the Fundamental Research Funds for the Central Universities (grant No.19CX05001A). Y.Z. thanks the Chinese government for the China Scholarship Council Award.

References

[1] D. Zhao, M. Dai, H. Liu, L. Xiao, X. Wu, H. Xia, Constructing High Performance Hybrid Battery and Electrocatalyst by Heterostructured $NiCo_2O_4$@NiWS Nanosheets, Cryst. Growth Des. 19 (2019) 1921-1929.

[2] L. Chirinos, N. L. Rose, R. Urrutia, P. Munoz, F. Torrejon, L. Torres, F. Cruces, A. Araneda, C. Zaror, Environmental evidence of fossil fuel pollution in Laguna Chica de San Pedro lake sediments (Central Chile), Environ. Pollut. 141 (2006) 247-256.

[3] F. Perera, Pollution from Fossil-Fuel Combustion is the Leading Environmental Threat to Global Pediatric Health and Equity: Solutions Exist, Int. J. Environ. Res. Public Health 15 (2017) 1-17.

[4] C. Liu, F. Li, L. P. Ma, H. M. Cheng, Advanced materials for energy storage, Adv. Mater. 22 (2010) E28-E62.

[5] G. Wang, L. Zhang, J. Zhang, A review of electrode materials for electrochemical supercapacitors, Chem. Soc. Rev. 41 (2012) 797-828.

[6] D. Zhao, H. Liu, X. Wu, Bi-interface induced multi-active MCo_2O_4@MCo_2S_4@PPy (M=Ni, Zn) sandwich structure for energy storage and electrocatalysis, Nano Energy 57 (2019) 363-370.

[7] C. Wu, T. Zhou, Y. Du, S. Dou, H. Zhang, L. Jiang, Q. Cheng, Strong bioinspired HPA-rGO nanocomposite films via interfacial interactions for flexible supercapacitors, Nano Energy 58 (2019) 517-527.

[8] P. Sharma, T. S. Bhatti, A review on electrochemical double-layer capacitors, Energy Convers. Manage. 51 (2010) 2901-2912.

[9] Y. Zhang, H. Feng, X. Wu, L. Wang, A. Zhang, T. Xia, H. Dong, X. Li, L. Zhang, Progress of electrochemical capacitor electrode materials: A review, Int. J. Hydrogen Energy 34 (2009) 4889-4899.

[10] W. Cui, M. Li, J. Liu, B. Wang, C. Zhang, L. Jiang, Q. Cheng, A Strong Integrated Strength and Toughness Artificial Nacre Based on Dopamine Cross-Linked Graphene Oxide, ACS Nano 8 (2014) 9511-9517.

[11] Y. Zhang, Y. Li, P. Ming, Q. Zhang, T. Liu, L. Jiang, Q. Cheng, Ultrastrong Bioinspired Graphene-Based Fibers via Synergistic Toughening, Adv. Mater. 28 (2016) 2834-2839.

[12] X. Zhang, X. Zeng, M. Yang, Y. Qi, Investigation of a Branchlike MoO_3/polypyrrole hybrid with enhanced electrochemical performance used as an electrode in supercapacitors, ACS Appl. Mater. Interfaces 6 (2014) 1125-30.

[13] D. Ghosh, S. Giri, M. Mandal, C. K. Das, High performance supercapacitor electrode material based on vertically aligned PANI grown on reduced graphene oxide/$Ni(OH)_2$ hybrid composite, RSC Adv. 4 (2014) 26094-26101.

[14] M. Yan, Y. Yao, J. Wen, L. Long, M. Kong, G. Zhang, X. Liao, G. Yin, Z. Huang, Construction of a Hierarchical $NiCo_2S_4$@PPy Core-Shell Heterostructure Nanotube Array on Ni Foam for a High-Performance Asymmetric Supercapacitor, ACS Appl. Mater. Interfaces 8 (2016) 24525-24535.

[15] W. Jiang, F. Hu, Q. Yan, X. Wu, Investigation on electrochemical behaviors of $NiCo_2O_4$ battery-type supercapacitor electrodes: the role of an aqueous electrolyte, Inorg. Chem. Front. 4 (2017) 1642-1648.

[16] C. Liu, W. Jiang, F. Hu, X. Wu, D. Xue, Mesoporous $NiCo_2O_4$ nanoneedle arrays as supercapacitor electrode materials with excellent cycling stabilities, Inorg. Chem. Front. 5 (2018) 835-843.

[17] Q. Cheng, M. Wu, M. Li, L. Jiang, Z. Tang, Ultratough artificial nacre based on conjugated cross-linked graphene oxide, Angew. Chem. Int. Ed. 52 (2013) 3750-3755.

[18] J. Wang, K. Y. Ma, J. Zhang, F. Liu, J. P. Cheng, Template-free synthesis of hierarchical hollow NiS_x microspheres for supercapacitor, J. Colloid Interface Sci. 507 (2017) 290-299.

[19] X. Li, J. Shen, N. Li, M. Ye, Template-free solvothermal synthesis of NiS_2 microspheres on graphene sheets for high-performance supercapacitors, Mater. Lett. 139 (2015) 81-85.

[20] R. Ren, M. S. Faber, R. Dziedzic, Z. Wen, S. Jin, S. Mao, J. Chen, Metallic CoS_2 nanowire electrodes for high cycling performance supercapacitors, Nanotechnology 26 (2015) 494001.

[21] Q. Wang, L. Jiao, H. Du, W. Peng, Y. Han, D. Song, Y. Si, Y. Wang, H. Yuan, Novel flower-like CoS hierarchitectures: one-pot synthesis and electrochemical properties, J. Mater. Chem. 21 (2011) 327-329.

[22] B. Wei, H. Liang, R. Wang, D. Zhang, Z. Qi, Z. Wang, One-step synthesis of graphitic-C_3N_4/ZnS composites for enhanced supercapacitor performance, J. Energ. Chem. 27 (2018) 472-477.

[23] R. Ramachandran, M. Saranya, P. Kollu, B. P. C. Raghupathy, S. K. Jeong, A. N. Grace, Solvothermal synthesis of Zinc sulfide decorated Graphene (ZnS/G) nanocomposites for novel Supercapacitor electrodes, Electrochim. Acta 178 (2015) 647-657.

[24] H. Yan, T. Li, Y. Lu, J. Cheng, T. Peng, J. Xu, L. Yang, X. Hua, Y. Liu, Y. Luo, Template-free synthesis of ordered ZnO@ZnS core-shell arrays for high performance supercapacitors, Dalton Trans. 45 (2016) 17980-17986.

[25] L. S. C. N. Sabari Arul, Jeong In Han, Facile synthesis of ZnS/MnS nanocomposites for supercapacitor applications, J. Solid State Electr. *22* (2017) 303-313.

[26] J. Pu, F. Cui, S. Chu, T. Wang, E. Sheng, Z. Wang, Preparation and Electrochemical Characterization of Hollow Hexagonal $NiCo_2S_4$ Nanoplates as Pseudocapacitor Materials, ACS Sustain. Chem. Eng. 2 (2013) 809-815.

[27] C. Liu, X. Wu, $NiCo_2S_4$ nanotube arrays grown on flexible carbon fibers as battery-type electrodes for asymmetric supercapacitors, Mater. Res. Bull. 103 (2018) 55-62.

[28] C. Liu, X. Wu, H. Xia, Flexible Mn-decorated $NiCo_2S_4$ core–shell nanowire arrays for a high performance hybrid supercapacitor electrode with a long cycle life, CrystEngComm 20 (2018) 4735-4744.

[29] W. Xu, J. Lu, W. Huo, J. Li, X. Wang, C. Zhang, X. Gu, C. Hu, Direct growth of CuCo2S4 nanosheets on carbon fiber textile with enhanced electrochemical pseudocapacitive properties and electrocatalytic properties towards glucose oxidation, Nanoscale 10 (2018) 14304-14313.

[30] M. Yu, X. Li, Y. Ma, R. Liu, J. Liu, S. Li, Nanohoneycomb-like manganese cobalt sulfide/three dimensional graphene-nickel foam hybid electrodes for high-rate capability supercapacitors, Appl. Surf. Sci. 396 (2017) 1816-1824.

[31] G. Huang, T. Chen, Z. Wang, K. Chang, W. Chen, Synthesis and electrochemical performances of cobalt sulfides/graphene nanocomposite as anode material of Li-ion battery, J. Power Sources 235 (2013) 122-128.

[32] B. Chen, R. Li, G. Ma, X. Gou, Y. Zhu, Y. Xia, Cobalt sulfide/N,S codoped porous carbon core-shell nanocomposites as superior bifunctional electrocatalysts for oxygen reduction and evolution reactions, Nanoscale 7 (2015) 20674-20684.

[33] N. Cao, Y. Zhang, Study of Reduced Graphene Oxide Preparation by Hummers' Method and Related Characterization, J. Nanomater. 2015 (2015) 1-5.

[34] S. Chen, J. Duan, Y. Tang, S. Z. Qiao, Hybrid hydrogels of porous graphene and nickel hydroxide as advanced supercapacitor materials, Chem. 19 (2013) 7118-7124.

[35] K. Subramani, N. Sudhan, R. Divya, M. Sathish, All-solid-state asymmetric supercapacitors based on cobalt hexacyanoferrate-derived CoS and activated carbon, RSC Adv. 7 (2017) 6648-6659.

[36] J. S. Xiuxia Li, Liya Feng, Lijun Zhao, Lin Ye, Wenqi Zhang, Lianfeng Duan, Cactus-like ZnS/Ni_3S_2 hybrid with high electrochemical performance for supercapacitors, J. Alloys Compd. 753 (2018) 508-516.

[37] S. S. Raut, B. R. Sankapal, First report on synthesis of $ZnFe_2O_4$ thin film using successive ionic layer adsorption and reaction: Approach towards solid-state symmetric supercapacitor device, Electrochim. Acta 198 (2016) 203-211.

[38] J. S. S. Umakant M. Patil, Sachin B. Kulkarni, Su Chan Lee, Hyung Goo Park, Kishor V. Gurav, J.H. Kim, and Seong Chan Jun, Enhanced Supercapacitive Performance of Chemically Grown Cobalt−Nickel Hydroxides on Three-Dimensional Graphene Foam Electrodes, ACS Appl. Mater. Interfaces 6 (2014) 2450-2458.

[39] Y. Liu, J. Zhang, S. Wang, K. Wang, Z. Chen, Q. Xu, Facilely constructing 3D porous $NiCo_2S_4$ nanonetworks for high-performance supercapacitors, New J. Chem. 38 (2014) 4045-4048.

[40] X. Chen, D. Chen, X. Guo, R. Wang, H. Zhang, Facile Growth of Caterpillar-like $NiCo_2S_4$ Nanocrystal Arrays on Nickle Foam for High-Performance Supercapacitors, ACS Appl. Mater. Interfaces 9 (2017) 18774-18781.

[41] M. S. Javed, J. Chen, L. Chen, Y. Xi, C. Zhang, B. Wan, C. Hu, Flexible full-solid state supercapacitors based on zinc sulfide spheres growing on carbon textile with superior charge storage, J. Mater. Chem. A 4 (2016) 667-674.

[42] B. Sarma, R. S. Ray, M. Misra, Charge storage in flower-like ZnS electrochemically deposited on TiO_2 nanotube, Mater. Lett. 139 (2015) 77-80.

[43] C. Cheng, D. Kong, C. Wei, W. Du, J. Zhao, Y. Feng, Q. Duan, Self-template synthesis of hollow ellipsoid Ni-Mn sulfides for supercapacitors, electrocatalytic oxidation of glucose and water treatment, Dalton Trans. 46 (2017) 5406-5413.

[44] Y. Zhu, Z. Wu, M. Jing, X. Yang, W. Song, X. Ji, Mesoporous $NiCo_2S_4$ nanoparticles as high-performance electrode materials for supercapacitors, J. Power Sources 273 (2015) 584-590.

[45] Y. Sui, Y. Zhang, H. Hu, Q. Xu, F. Yang, Z. Li, High Energy Density Asymmetric Supercapacitor Based $ZnS/NiCo_2S_4/Co_9S_8$ Nanotube Composites Materials, Adv. Mater. Interfaces 5 (2018) 1800018.

[46] Y. Zhu, X. Chen, W. Zhou, K. Xiang, W. Hu, H. Chen, Controllable preparation of highly uniform $CuCo_2S_4$ materials as battery electrode for energy storage with enhanced electrochemical performances, Electrochim. Acta 249 (2017) 64-71.

[47] S. Deng, D. Sun, C. Wu, H. Wang, J. Liu, Y. Sun, H. Yan, Synthesis and electrochemical properties of MnO_2 nanorods/graphene composites for supercapacitor applications, Electrochim. Acta 111 (2013) 707-712.

[48] Y. Chen, D. Ni, X. Yang, C. Liu, J. Yin, K. Cai, Microwave-assisted synthesis of honeycomblike hierarchical spherical Zn-doped Ni-MOF as a high-performance battery-type supercapacitor electrode material, Electrochim. Acta 278 (2018) 114-123.

[49] Z. Yang, C.-Y. Chen, H.-T. Chang, Supercapacitors incorporating hollow cobalt sulfide hexagonal nanosheets, J. Power Sources 196 (2011) 7874-7877.

[50] R. B. Rakhi, N. A. Alhebshi, D. H. Anjum, H. N. Alshareef, Nanostructured cobalt sulfide-on-fiber with tunable morphology as electrodes for asymmetric hybrid supercapacitors, J. Mater. Chem. A 2 (2014) 16190-16198.

[51] X. Wang, J. Hao, Y. Su, F. Liu, J. An, J. Lian, A $Ni_{1-x}Zn_xS$/Ni foam composite electrode with multi-layers: one-step synthesis and high supercapacitor performance, J. Mater. Chem. A 4 (2016) 12929-12939.

[52] C. Yuan, J. Li, L. Hou, X. Zhang, L. Shen, X. W. D. Lou, Ultrathin Mesoporous $NiCo_2O_4$ Nanosheets Supported on Ni Foam as Advanced Electrodes for Supercapacitors, Adv. Funct. Mater. 22 (2012) 4592-4597.

[53] X. Tian, C. Cheng, L. Qian, B. Zheng, H. Yuan, S. Xie, D. Xiao, M. M. F. Choi, Microwave-assisted non-aqueous homogenous precipitation of nanoball-like mesoporous α-$Ni(OH)_2$ as a precursor for NiO_x and its application as a pseudocapacitor, J. Mater. Chem. 22 (2012) 8029-8035.

[54] H. R. Naderi, P. Norouzi, M. R. Ganjali, Electrochemical study of a novel high performance supercapacitor based on MnO_2/nitrogen-doped graphene nanocomposite, Appl. Surf. Sci. 366 (2016) 552-560.

[55] S. Nandhini, A. J. C. Mary, G. Muralidharan, Facile microwave-hydrothermal synthesis of NiS nanostructures for supercapacitor applications, Appl. Surf. Sci. 449 (2018) 485-491.

[56] H. Wan, X. Ji, J. Jiang, J. Yu, L. Miao, L. Zhang, S. Bie, H. Chen, Y. Ruan, Hydrothermal synthesis of cobalt sulfide nanotubes: The size control and its application in supercapacitors, J. Power Sources 243 (2013) 396-402.

[57] R. K. G. Karthik Ramasamy, Hunter Sims, Soubantika Palchoudhury, Sergei Ivanova and Arunava Gupta, Layered ternary sulfide $CuSbS_2$ nanoplates for flexible solid-state supercapacitors, J. Mater. Chem. A 3 (2015) 13263-13274.

[58] W. Kong, C. Lu, W. Zhang, J. Pu, Z. Wang, Homogeneous core–shell $NiCo_2S_4$ nanostructures supported on nickel foam for supercapacitors, J. Mater. Chem. A 3 (2015) 12452-12460.